Time-Varying MIMO Channels: Parametric Statistical Modeling and Experimental Results

Shuangquan Wang*, *Student Member, IEEE,* Ali Abdi*, *Member, IEEE,* Jari Salo†, *Student Member, IEEE,* Hassan M. El-Sallabi†, *Member, IEEE,* Jon W. Wallace‡, *Member, IEEE,* Pertti Vainikainen†, *Member, IEEE,* Michael A. Jensen‡, *Senior Member, IEEE*

Abstract

Accurate characterization of multiple-input multiple-output (MIMO) fading channels is an important prerequisite for the design of multi-antenna wireless communication systems. In this paper, a *single-bounce two-ring* statistical model for time-varying MIMO flat fading channels is proposed. In the model, both the base and mobile stations are surrounded by their own ring of scatterers. For the proposed model, a closed-form expression for the spatio-temporal cross-correlation function between any two subchannels is derived, assuming single-bounce scattering. The new analytical expression includes several key physical parameters of interest such as the mean angle-of-departure, the mean angle-of-arrival, the associated angle spreads and the Doppler spread in a compact form. The model includes many existing correlation models as special cases. Its utility is demonstrated by a comparison with collected MIMO data in terms of the spatio-temporal correlations, level crossing rate, average fade duration, and the instantaneous mutual information.

Index Terms

Channel Modeling, Multiple Input Multiple Output (MIMO), Multi-Antenna Systems, Level Crossing Rate (LCR), Average Fade Duration (AFD), Spatio-Temporal Cross-Correlation (STCC), Instantaneous Mutual Information and Rayleigh Fading.

I. Introduction

The utilization of antenna arrays at the base station (BS) and the mobile station (MS) in a wireless communication system increases the capacity linearly with $\min(N_T, N_R)$, where N_T and N_R are numbers of transmit (Tx) and receive

This paper was presented in part at the *IEEE Sarnoff Symposium on Advances in Wired and Wireless Communications*, Princeton, NJ, 2004, and *IEEE International Workshop on Signal Processing Advances for Wireless Communications*, New York City, NY, 2005.

*S. Wang and A. Abdi are with the Center for Wireless Communications and Signal Processing Research (CWCSPR), Department of Electrical and Computer Engineering, New Jersey Institute of Technology, Newark, NJ 07102, USA (e-mail:{sw27, ali.abdi}@njit.edu).

†J. Salo, H. M. El-Sallabi and P. Vainikainen are with the Radio Laboratory, Helsinki University of Technology, P. O. Box 3000, FI-02015-TKK, Finland.

‡J. W. Wallace and M. A. Jensen are with the Department of Electrical and Computer Engineering, Brigham Young University, Provo, UT 84602, USA.

(Rx) antenna elements, respectively, provided that the environment is sufficiently rich in multi-path components [1][2]. The significant increase of channel capacity was originally reported for uncorrelated subchannels[1] [1][2]. However, later it was realized that the correlation among subchannels can significantly affect capacity [3]–[6] and other system performance metrics [7]–[10]. For an overview of MIMO channel models, the readers can refer to [11]–[14] and references therein. In this paper, we concentrate on statistical modeling of time-varying MIMO flat[2] fading channels and verify the utility of the proposed model via comparison with different sets of data.

In a typical macrocell, the BS is elevated and receives the signal within a narrow beamwidth, whereas the MS is surrounded by local scatterers. MIMO modeling of this typical macrocell environment is investigated in [3], where a closed-form expression for the MIMO spatio-temporal cross-correlation (STCC) is derived, assuming non-isotropic scattering around the MS. However, in outdoor microcells and indoor picocells, both the BS and MS are normally surrounded by local scatterers. Clearly, the MIMO macrocell model of [3] cannot be used for such environments. For this situation, we need a double-directional channel model (see [15] and [16], where the double-directional concept is introduced and some measurements results are provided).

In this paper the space-time model of [3] is extended by adding another ring of scatterers around the BS in order to facilitate a new and mathematically tractable MIMO STCC model needed for analytical calculations and system design, for example, array optimization [17]. We call the newly extended model the *single-bounce two-ring* model since only single-bounce rays are considered. The proposed model includes [3] and some other existing correlation models as special cases. Note that the proposed model belongs to the class of double-directional channel models since it includes angular information at both the BS and MS. Most importantly, the proposed parametric model provides a compact analytical form for MIMO STCC in terms of several key physical parameters of the channel. It also avoids the technical difficulties of the double-bounce two-ring model (e.g. [18]) discussed in [11]. The parametric nature of the model makes it adaptable to a variety of propagation environments, and its compact mathematical form is convenient for both analytical studies and numerical calculations. Finally, comparison of the model with the data collected at Helsinki University of Technology (HUT) [19][20] and Brigham Young University (BYU) [21][22] confirms the utility of the model in real environments in terms of mutual information, several types of correlations, level crossing rate (LCR) and average fade duration (AFD).

The rest of the paper is organized as follows. The *single-bounce two-ring* model is presented in Section II. The closed-form expression for the spatio-temporal cross-correlation function between any two subchannels is derived in Section III. Section IV includes data processing and parameter estimation techniques. In Section V, we compare the proposed model with measured data from HUT and BYU, whose details are given in Appendix II and III. Finally, concluding remarks are provided in Section VI.

Notation: $\|\cdot\|_F$ is reserved for the Frobenius norm, $(\cdot)^\dagger$ for the matrix Hermitian, $(\cdot)^T$ for the matrix transpose,

[1]In this paper, each subchannel represents the radio link between each Tx/Rx pair of antennas with the time-varying gain in (2).

[2]Only the flat fading is considered here since the MIMO frequency-selective fading channel can be converted into several flat fading channels by the orthogonal frequency division multiplexing (OFDM) technique.

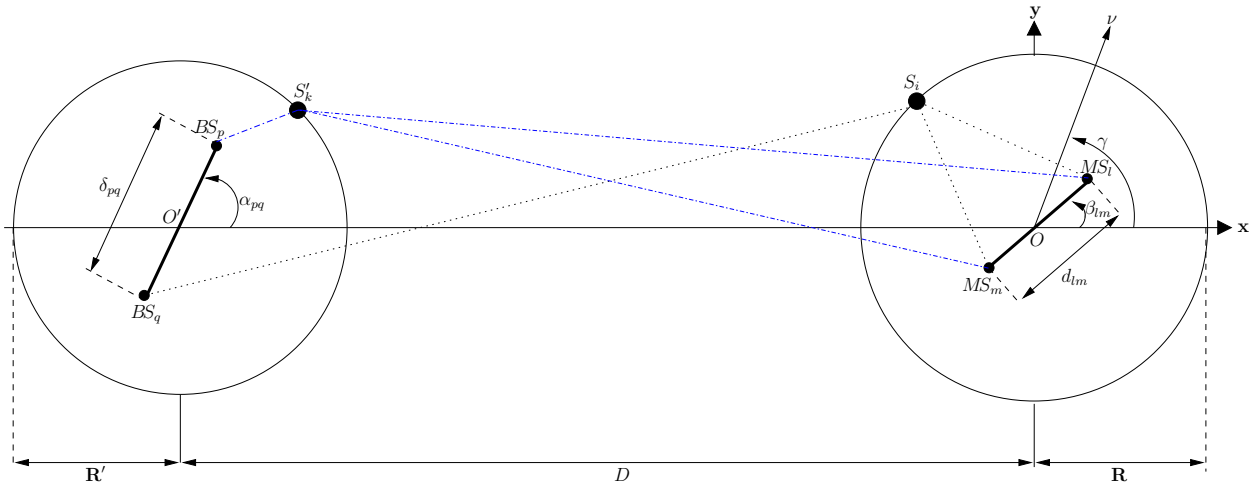

Fig. 1. Geometrical configuration of a 2×2 channel with local scatterers around the MS and BS, with some single-bounce rays shown in the forward channel.

$(\cdot)^\star$ for the complex conjugate, $\mathbb{E}[\cdot]$ for the mathematical expectation, and $\jmath$ for $\sqrt{-1}$. $\mathbf{I}_m$ denotes the $m \times m$ identity matrix, and $[\mathbf{A}]_{m,n}$ is the $(m,n)^{\text{th}}$ element of the matrix $\mathbf{A}$. $t \in [m,n]$ with integers m and n implies that t is an integer such that $m \leqslant t \leqslant n$, whereas $t \in [z_1, z_2)$ with real z_1 and z_2 denotes that t is real such that $z_1 \leqslant t < z_2$. $\min(x,y)$ and $\max(x,y)$ indicate the minimum and maximum of real x and y, respectively. vec$(\mathbf{A})$ stacks all the columns of the matrix $\mathbf{A}$ into one tall column vector.

II. The Proposed Statistical Model

For a linear time-varying flat fading $N_R \times N_T$ MIMO system, the input-output relationship can be written as

$$\mathbf{r}(t) = \sqrt{\frac{P_{\text{Tx}}}{N_T}}\mathbf{H}(t)\mathbf{s}(t) + \mathbf{e}(t). \tag{1}$$

In (1) P_{Tx} is the total emitted power from the Tx antenna array. $[\mathbf{H}(t)]_{l,p} = h_{lp}(t)$, $h_{lp}(t)$ denotes the complex baseband equivalent channel gain between the p^{th} transmitter and l^{th} receiver. $\mathbf{r}(t) = [r_1(t), r_2(t), \cdots, r_{N_R}(t)]^T$ is the received signal vector at time t. $\mathbf{s}(t) = [s_1(t), s_2(t), \cdots, s_{N_T}(t)]^T$ is the transmitted symbol vector from N_T Tx antennas at time t such that each element of $\mathbf{s}(t)$ has unit power. $\mathbf{e}(t) = [e_1(t), e_2(t), \cdots, e_{N_R}(t)]^T$ is the additive white Gaussian noise (AWGN) vector with the covariance matrix $\mathbf{R} = \mathbb{E}[\mathbf{e}(t)\mathbf{e}^\dagger(t)] = P_{\text{Noise}}\mathbf{I}_{N_R}$ [3], where P_{Noise} is the average noise power at each Rx antenna element.

The geometry of the proposed model is shown in Fig. 1 for a 2×2 channel where scatterers local to the BS and MS are modeled to be distributed on two separate rings. The key difference between our model and the other two-ring model [11] is that only single-bounce rays are considered, and multiple bounces are treated as secondary effects. This avoids the problem of the double-bounce two-ring model discussed in [11], facilitates the derivation of closed-form results, and proves to be a useful approximation when compared with measured data.

In Fig. 1, the forward channel (from the BS to the MS), the MS receives single-bounce rays from the scatterer S_i around the MS (shown by dotted lines) and the scatterer S'_k around the BS (shown by dash-dotted lines). D is the distance between the MS and BS, R and R' are the radii of the scattering rings around the MS and BS, respectively, and α_{pq} and β_{lm} are the directions of the subarray BS_p-BS_q with element spacing δ_{pq}, and subarray MS_l-MS_m with element spacing d_{lm}, respectively[3]. For the frequency flat subchannel between the antenna elements BS_p and MS_l, $h_{lp}(t)$ denotes the time-varying complex baseband equivalent channel gain. Mathematical representation of the superposition of rays at the MS results in the following expression for the channel gain[4]

$$h_{lp}(t)=\sqrt{\eta'\Omega_{lp}}\sum_{k=1}^{N'}\frac{g'_k}{\sqrt{N'}}\exp\Big[\jmath\psi'_k-\frac{\jmath 2\pi}{\lambda}(\xi'_{pk}+\xi'_{kl})+\jmath 2\pi f_D\cos(\varphi'_k-\gamma)t\Big] + \sqrt{\eta\Omega_{lp}}\sum_{i=1}^{N}\frac{g_i}{\sqrt{N}}\exp\Big[\jmath\psi_i-\frac{\jmath 2\pi}{\lambda}(\xi_{pi}+\xi_{il})+\jmath 2\pi f_D\cos(\phi_i-\gamma)t\Big], \quad (2)$$

where the first and second summations correspond to the BS and MS rings, respectively. From (2), it is clear that the angle of arrival (AoA) and angle of departure (AoD) play the interrelation between the *single-bounce two-ring* model in Fig. 2 and the channel transfer function $\mathbf{H}(t)$ in (1).

In (2), Ω_{lp} is the power transmitted through the subchannel $\mathrm{BS}_p-\mathrm{MS}_l$, i.e., $\Omega_{lp}=\mathbb{E}\big[|h_{lp}|^2\big]$, η' and η show the respective contributions of scatterers around BS and MS to Ω_{lp} such that $\eta'+\eta=1$, N and N' are numbers of scatterers around the MS and BS, respectively. The positive random variables g_i and g'_k represent the amplitudes of the waves scattered by S_i and S'_k, which also include the antenna gains at ϕ_i and ϕ'_k, and ψ_i and ψ'_k are the associated phase shifts. Furthermore, as shown in Fig. 2, ϕ'_k and φ_i are AoD's of the waves that impinge on S'_k and S_i, whereas φ'_k and ϕ_i are AoA's of the waves scattered from S'_k and S_i. ξ'_{pk} and ξ'_{qk}, functions of ϕ'_k, are the lengths of BS_p-S'_k and BS_q-S'_k links, respectively, whereas ξ'_{kl} and ξ'_{km}, functions of φ'_k, are the lengths of S'_k-MS_l and S'_k-MS_m links. Other ξ's can be easily identified in Fig. 2 and their functional relationships are given in (26a)-(26h). Finally, λ, f_D, and γ are the wavelength, maximum Doppler frequency, and the direction of the MS motion, respectively.

The sets $\{g_i\}_{i=1}^{N}$ and $\{g'_k\}_{k=1}^{N'}$ consist of independent positive random variables with finite variances, independent of $\{\psi_i\}_{i=1}^{N}$ and $\{\psi'_k\}_{k=1}^{N'}$. We assume $\{\psi_i\}_{i=1}^{N}$ and $\{\psi'_k\}_{k=1}^{N'}$ are independent and identically distributed (i.i.d) random variables with uniform distributions over $[0,2\pi)$. We also set $N^{-1}\sum_{i=1}^{N}\mathbb{E}\big[g_i^2\big]=1$ and $N'^{-1}\sum_{k=1}^{N'}\mathbb{E}\big[g_k'^2\big]=1$, which result in the desired identity $\mathbb{E}\big[|h_{lp}(t)|^2\big]=\Omega_{lp}$. The second moments of $g_i,\forall i$ and $g'_k,\forall k$ will be discussed in Section III. According to Fig. 2, φ_i is a function of ϕ_i and φ'_k is a function of ϕ'_k, therefore, only ϕ'_k and ϕ_i are independent angular variables. In what follows, we call ϕ'_k the AoD, and ϕ_i the AoA.

[3]Note that $\alpha_{qp}=\alpha_{pq}+\pi, p<q$, $\beta_{ml}=\beta_{lm}+\pi, l<m$, $\delta_{pq}=\delta_{qp}\geqslant 0,\forall p,q$, and $d_{lm}=d_{ml}\geqslant 0,\forall l,m$, with p,q,l,m being positive integers.

[4]To save space, only non line-of-sight (NLOS) components are considered in (2). It can be easily extended to include the line-of-sight (LOS) component by introducing Rician K factor if the number of scatters is large, in the same way as in [3].

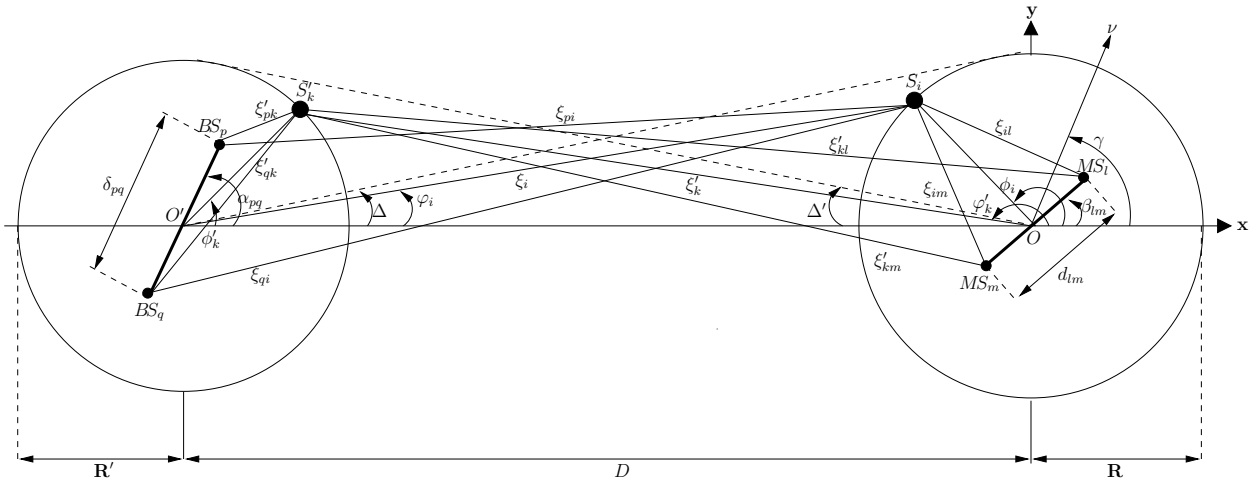

Fig. 2. Detailed version of Fig. 1.

III. The MIMO Spatio-Temporal Cross-Correlation

Based on the independent properties of g_i's, g'_k's, ψ_i's and ψ'_k's, the normalized STCC between two subchannel gains $h_{lp}(t)$ and $h_{mq}(t)$, defined as $\rho_{lp,mq}(\tau) = \mathbb{E}[h_{lp}(t+\tau)h^{\star}_{mq}(t)]/\sqrt{\Omega_{lp}\Omega_{mq}}$ [5], can be asymptotically written as

$$\rho_{lp,mq}(\tau) = \lim_{N'\to\infty} \frac{(1-\eta)}{N'} \sum_{k=1}^{N'} \mathbb{E}\big[g'^2_k\big] \exp\Big[-\jmath\frac{2\pi}{\lambda}(\xi'_{pk}-\xi'_{qk}+\xi'_{kl}-\xi'_{km}) + \jmath 2\pi f_D \cos(\varphi'_k-\gamma)\tau\Big] + \lim_{N\to\infty} \frac{\eta}{N} \sum_{i=1}^{N} \mathbb{E}\big[g_i^2\big] \exp\Big[-\jmath\frac{2\pi}{\lambda}(\xi_{pi}-\xi_{qi}+\xi_{il}-\xi_{im})+\jmath 2\pi f_D \cos(\phi_i-\gamma)\tau\Big]. \quad (3)$$

For large N' and N, the small amounts of power received from S'_k and S_i are proportional to $N'^{-1}\mathbb{E}\big[g'^2_k\big]$ and $N^{-1}\mathbb{E}\big[g_i^2\big]$, respectively. They are also equal to the infinitesimal powers through the differential angles $d\phi'$ and $d\phi$ with probabilities $f_{\mathrm{BS}}(\phi'_k)d\phi'$ and $f_{\mathrm{MS}}(\phi_i)d\phi$, respectively. This implies that $N'^{-1}\mathbb{E}\big[g'^2_k\big] = f_{\mathrm{BS}}(\phi'_k)d\phi'$ and $N^{-1}\mathbb{E}\big[g_i^2\big] = f_{\mathrm{MS}}(\phi_i)d\phi$, where $f_{\mathrm{BS}}(\cdot)$ is the probability density functions (PDF) of the AoD, and $f_{\mathrm{MS}}(\cdot)$ is the PDF of the AoA. To simplify the notation, we define $x=\phi'_k$, $y=\phi_i$, $v=\varphi'_k$, and $w=\varphi_i$. Therefore, (3) can be reduced to the following integral form

$$\rho_{lp,mq}(\tau) = (1-\eta)\int_{-\pi}^{\pi} \exp\Big[-\frac{\jmath 2\pi}{\lambda}(\xi'_{px}-\xi'_{qx}+\xi'_{xl}-\xi'_{xm}) + \jmath 2\pi f_D \cos(v-\gamma)\tau\Big] f_{\mathrm{BS}}(x)dx + \eta\int_{-\pi}^{\pi} \exp\Big[-\frac{\jmath 2\pi}{\lambda}(\xi_{py}-\xi_{qy}+\xi_{yl}-\xi_{ym}) + \jmath 2\pi f_D \cos(y-\gamma)\tau\Big] f_{\mathrm{MS}}(y)dy, \quad (4)$$

where ξ''s depend on ϕ'_k, and ξ's depend on ϕ_i according to Fig. 2.

For any given $f_{\mathrm{BS}}(\cdot)$ and $f_{\mathrm{MS}}(\cdot)$, (4) can be calculated numerically, using the trigonometric function relationships given in (26a)-(26h), (30a) and (30b). Note that (4) includes two parts, the first one corresponds to the STCC

[5]This definition is the same as the one in [3] if τ is replaced by $-\tau$.

contributed by the scattering ring around the BS, and the second is from the scattering ring around the MS.

In order to further simplify (4), similarly to [3], the assumptions of $D \gg \max(R', R)$, $R' \gg \delta_{pq}$ and $R \gg d_{lm}$ are made[6]. With these assumptions and the identities given in (26a)-(26h), (4) can be approximated by

$$\rho_{lp,mq}(\tau) \approx (1-\eta)\int_{-\pi}^{\pi} \exp\Big\{\jmath 2\pi\big[\delta_{pq}\cos(\alpha_{pq}-x) + d_{lm}\cos(v-\beta_{lm})\big]/\lambda + \jmath 2\pi f_D \cos(v-\gamma)\tau\Big\} f_{\rm BS}(x)dx + \eta\int_{-\pi}^{\pi} \exp\Big\{\jmath 2\pi\big[\delta_{pq}\cos(\alpha_{pq}-w) + d_{lm}\cos(y-\beta_{lm})\big]/\lambda + \jmath 2\pi f_D \cos(y-\gamma)\tau\Big\} f_{\rm MS}(y)dy. \quad (5)$$

The details of the derivation are given in Appendix I.

In this paper, we consider the empirically-verified von Mises angular PDF [23] for both the AoD and AoA[7]. They are given by

$$f_{\rm BS}(x) = \frac{\exp[\kappa'\cos(x-\mu')]}{2\pi I_0(\kappa')}, \quad x \in [0, 2\pi), \quad (6a)$$

$$f_{\rm MS}(y) = \frac{\exp[\kappa\cos(y-\mu)]}{2\pi I_0(\kappa)}, \quad y \in [0, 2\pi). \quad (6b)$$

In (6a) and (6b), $I_k(z) = \frac{1}{\pi}\int_0^{\pi} e^{z\cos\theta}\cos(k\theta)d\theta$ is the $k^{\rm th}$ order modified Bessel function of the first kind, μ' and μ account for the mean AoD and mean AoA, respectively, and κ' and κ ($\geqslant 0$) control the angular spreads of the AoD and AoA, respectively. If $\kappa = \kappa' = 0$, both PDF's in (6) simplify to $\frac{1}{2\pi}$, which represents isotropic scattering. As will be seen in Appendix I, the mathematical form of the von Mises PDF is convenient for analytic calculations and derivations of closed-form expressions.

Based on (30a), (30b), (33) and the assumption of $D \gg \max(R', R)$, the following closed-form expression for the spatio-temporal cross-correlation is derived in Appendix I

$$\rho_{lp,mq}(\tau) \approx (1-\eta)\frac{\exp\left[-\jmath(b_{lm}\cos\beta_{lm} - a\cos\gamma)\right]}{I_0(\kappa')} I_0\Big(\big\{\kappa'^2 - a^2\Delta'^2\sin^2\gamma - b_{lm}^2\Delta'^2\sin^2\beta_{lm} - c_{pq}^2 - 2b_{lm}c_{pq}\Delta'\sin\alpha_{pq}\sin\beta_{lm} + 2a\Delta'\sin\gamma(c_{pq}\sin\alpha_{pq} + b_{lm}\Delta'\sin\beta_{lm}) - \jmath 2\kappa'[a\Delta'\sin\mu'\sin\gamma - b_{lm}\Delta'\sin\beta_{lm} \times \sin\mu' - c_{pq}\cos(\alpha_{pq}-\mu')]\big\}^{\frac{1}{2}}\Big) + \eta\frac{\exp(\jmath c_{pq}\cos\alpha_{pq})}{I_0(\kappa)} I_0\Big(\big\{\kappa^2 - a^2 - b_{lm}^2 - c_{pq}^2\Delta^2\sin^2\alpha_{pq} + 2c_{pq}\Delta\sin\alpha_{pq} \times (a\sin\gamma - b_{lm}\sin\beta_{lm}) + 2ab_{lm}\cos(\beta_{lm}-\gamma) - \jmath 2\kappa[a\cos(\mu-\gamma) - b_{lm}\cos(\beta_{lm}-\mu) - c_{pq}\Delta\sin\alpha_{pq}\sin\mu]\big\}^{\frac{1}{2}}\Big). \quad (7)$$

Here we have $a = -2\pi f_D\tau$, $b_{lm} = 2\pi d_{lm}/\lambda$ and $c_{pq} = 2\pi\delta_{pq}/\lambda$. Furthermore, $2\Delta'$ is the maximum angle spread at the MS, determined by the scattering ring around the BS. Similarly, 2Δ is the maximum angle spread at the BS, dictated by the scattering ring around the MS. Note that (7) is a closed-form STCC function between any two subchannels of a MIMO system with arbitrary array configurations, i.e., Tx and Rx arrays do not have to be linear.

[6]These assumptions can be justified in many propagation scenarios of practical interest. In certain picocell propagation environments, however, $D \gg \max(R', R)$ may not strictly hold. This may result in some discrepancies between the model and measured data in some cases, as discussed in Subsection V-E.

[7]In this paper, no preassumption is made about the antenna patterns. In fact, g_k''s and g_i's include the Tx and Rx antenna gains, and the angular PDF's in (6a) and (6b) include the effect of antenna patterns.

In what follows, we show many existing correlation models can be considered as special cases of (7).

- If there is no scatterer around the BS as in a macrocell ($\eta = 1$), the first half of (7) disappears, and the remaining part is the same as (12) in [3], when τ is changed to[5] $-\tau$. It implies that (7) includes the model of [3] and subsequently other models listed in [3] as special cases.
- With $l = m$ and $p = q$, the temporal autocorrelation of the subchannel $h_{lp}(t)$ can be derived from (7) as

$$\rho(\tau) = (1-\eta)\exp(\jmath a\cos\gamma)\frac{I_0\Big(\sqrt{\kappa'^2 - a^2\Delta'^2\sin^2\gamma - \jmath 2\kappa' a\Delta'\sin\mu'\sin\gamma}\Big)}{I_0(\kappa')} + \frac{\eta I_0\Big(\sqrt{\kappa^2 - a^2 - \jmath 2\kappa a\cos(\mu-\gamma)}\Big)}{I_0(\kappa)}, \quad (8)$$

  where $\rho(\tau) = \rho_{lp,lp}(\tau), \forall l, p$. If $\eta = 1$, (8) reduces to the model of [23].

  – With $\eta = 1$ and $\kappa = 0$ (isotropic scattering around the MS), (8) simplifies to the well-known Clarke's temporal correlation model, i.e., $J_0(2\pi f_D\tau)$ [24], where $J_0(\cdot)$ is the Bessel function of the first kind of order zero.

- When the MS does not move, for example, in indoor environments, one gets $f_D = 0$. This reduces (7) to the following spatial correlation between h_{lp} and h_{mq}

$$\rho_{lp,mq} = (1-\eta)\frac{e^{-\jmath b_{lm}\cos\beta_{lm}}}{I_0(\kappa')} I_0\Big(\big\{\kappa'^2 - b_{lm}^2\Delta'^2\sin^2\beta_{lm} - c_{pq}^2 - 2b_{lm}c_{pq}\Delta'\sin\alpha_{pq}\sin\beta_{lm} + \jmath 2\kappa'[b_{lm}\Delta'\sin\beta_{lm} \times \sin\mu' + c_{pq}\cos(\alpha_{pq}-\mu')]\big\}^{\frac{1}{2}}\Big) + \eta\frac{e^{\jmath c_{pq}\cos\alpha_{pq}}}{I_0(\kappa)} I_0\Big(\big\{\kappa^2 - b_{lm}^2 - c_{pq}^2\Delta^2\sin^2\alpha_{pq} - 2b_{lm}c_{pq}\Delta\sin\alpha_{pq}\sin\beta_{lm} + \jmath 2\kappa[b_{lm}\cos(\beta_{lm}-\mu) + c_{pq}\Delta\sin\alpha_{pq}\sin\mu]\big\}^{\frac{1}{2}}\Big). \quad (9)$$

  – With isotropic scattering around both the BS and MS ($\kappa' = \kappa = 0$), and parallel linear arrays ($\alpha_{pq} = \beta_{lm} = \frac{\pi}{2}, \forall p, q, l, m$), the spatial correlation in (9) further simplifies to

$$\rho_{lp,mq} = (1-\eta)J_0(b_{lm}\Delta' + c_{pq}) + \eta J_0(b_{lm} + c_{pq}\Delta). \quad (10)$$

    * With $p = q$ and $\eta = 1$, (10) reduces to $\rho_{lp,mp} = J_0(2\pi d_{lm}/\lambda)$. It is the spatial correlation at the MS in a macrocell [24].
    * On the other hand, with $l = m$ and $\eta = 1$, (10) simplifies to $\rho_{lp,lq} = J_0(\Delta 2\pi\delta_{pq}/\lambda)$. It is the spatial correlation at the BS in a macrocell [25].

IV. Data Processing and Parameter Estimation

This section explains how the raw data are processed and how the parameters of the proposed model are estimated.

A. Normalization

First it is necessary to do some power normalization. In [26], the normalization is done according to $\widetilde{\mathbf{H}}(t) = \sqrt{N_T N_R}\mathbf{H}(t)/\left\|\mathbf{H}(t)\right\|_F$ for each t, $t \in [1, T]$, where $\mathbf{H}(t)$ is a snapshot of the channel matrix at time instant t, T

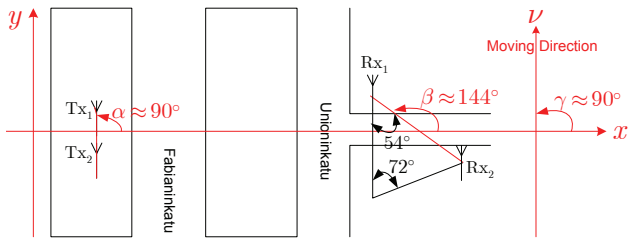

Fig. 3. Estimating α, β and γ by a comparison of Figs. 12 and 13 with Fig. 1.

is the total number of snapshots, and $\|\mathbf{H}(t)\|_F = \sqrt{\sum_{l=1}^{N_R}\sum_{p=1}^{N_T}|h_{lp}(t)|^2}$. Note that $\mathbf{H}(t)$ denotes $\mathbf{H}(tT_s)$ and T_s is the sampling period. To simplify notations, T_s is dropped in this section. In [27], normalization is intended to guarantee the so-called unit single-input single-output (SISO) gain, i.e., $T^{-1}\sum_{t=1}^{T}\left\|\widetilde{\mathbf{H}}(t)\right\|_F^2 = N_T N_R$, therefore, the normalization is done according to

$$\widetilde{\mathbf{H}}(t) = \sqrt{\frac{N_R N_T T}{\sum_{t=1}^{T}\|\mathbf{H}(t)\|_F^2}}\mathbf{H}(t), \quad t \in [1, T]. \tag{11}$$

According to our correlation model in (7), each individual subchannel has unit power. On the other hand, the above two normalization methods do not result in unit power for each subchannel. Hence, in this paper, normalization is performed such that each subchannel has unit variance and zero mean, i.e.,

$$\tilde{h}_{lp}(t) = \frac{h_{lp}(t) - \widehat{m}_{lp}}{\widehat{\sigma}_{lp}}, \quad \forall l, p, t, \tag{12}$$

where $\widehat{m}_{lp}$ and $\widehat{\sigma}_{lp}^2$ are the estimated mean and variance of the BS_p-MS_l subchannel. They are calculated from $\{h_{lp}(t)\}_{t=1}^{T}$ according to $\widehat{m}_{lp} = T^{-1}\sum_{t=1}^{T} h_{lp}(t)$ and $\widehat{\sigma}_{lp}^2 = T^{-1}\sum_{t=1}^{T}|h_{lp}(t) - \widehat{m}_{lp}|^2$.

B. Parameter Estimation

First we need to determine α and β, the directions of BS and MS arrays, respectively[8]. The direction of the MS motion γ and the Doppler drift f_D in the HUT data needs to be obtained as well, whereas the fixed MS in the BYU data does not need γ and f_D.

- For the HUT data, a comparison of Figs. 12 and 13 with Fig. 1 gives $\alpha = \frac{\pi}{2}$, $\beta = \frac{4\pi}{5}$ and $\gamma = \frac{\pi}{2}$. To obtain these angles, first x and y axes were chosen in the horizontal and vertical directions, respectively, similarly to Fig. 1, and were redrawn on Fig. 12. This results in Fig. 3. A comparison of Fig. 3 with Fig. 1 reveals that the BS array is parallel to the y axis, so, $\alpha = \frac{\pi}{2}$[9]. β can be determined similarly as $144^\circ = 180^\circ - (90 - 54)^\circ$, based on the 54° angle shown in Fig. 3. A further comparison of Fig. 3 with Fig. 1 shows that the mobile is moving parallel to the y axis in the positive direction. Therefore, $\gamma = \frac{\pi}{2}$. The data is taken over a $47m$

[8]In BYU measurements, both the Tx and Rx arrays are linear, and the HUT data used in this paper is a 2×2 channel taken from a large MIMO system. Therefore, in both measurement setups we have $\alpha_{pq} = \alpha$, $p < q$ and $\beta_{lm} = \beta$, $l < m$.

[9]Note that based on our convention, this α is indeed α_{12} (refer to footnote 8). As described in footnote 3, one cannot choose $\frac{3\pi}{2}$ for α_{12}. Therefore, based on our convention, $\alpha = \frac{\pi}{2}$ is the only choice in Fig. 3.

route in Unioninkatu Street, at the intersection with Rauhankatu Street, as shown in Fig. 12. $f_D = 2.872\,\text{Hz}$, which is derived in Appendix II. Note that only a small section ($\approx 20m$) around Rauhankatu Street is used. Therefore, the estimated α, β and γ is a fair approximation for all locations since $20m$ is small compared to the distance $150m$.

- Similarly, $\alpha = 168^{\text{o}}$ and $\beta = 78^{\text{o}}$ are obtained for the BYU data according to Figs. 1 and 14.

To estimate the rest of the parameters, $\mathbf{\Lambda} = (\Delta, \Delta', \kappa, \kappa', \mu, \mu', \eta)$, of the model, a nonlinear least-squares correlation fitting approach is used, via a numerical search over the parameter space. This is explained below.

For the BYU data, $\mathbf{\Lambda}$ is estimated[10] by fitting the spatial MIMO correlation matrix $\mathbf{R}(\mathbf{\Lambda})$, whose elements are given by (9), to the estimated spatial correlation matrix $\widehat{\mathbf{R}}$

$$\widehat{\mathbf{\Lambda}} = \arg\min_{\mathbf{\Lambda}} \left\| \widehat{\mathbf{R}} - \mathbf{R}(\mathbf{\Lambda}) \right\|_F^2 . \tag{13}$$

$\widehat{\mathbf{R}} = T^{-1} \sum_{t=1}^{T} \mathbf{h}(t)\mathbf{h}^{\dagger}(t)$ with $\mathbf{h}(t) = \text{vec}(\mathbf{H}(t))$. $\mathbf{R}(\mathbf{\Lambda}) = \mathbb{E}[\mathbf{h}(t)\mathbf{h}^{\dagger}(t)]$ such that $[\mathbf{R}(\mathbf{\Lambda})]_{l+N_R(p-1),m+N_R(q-1)}$ $= \rho_{lp,mq}, l, m \in [1, N_R]$, $p, q \in [1, N_T]$. Note that the expectation is taken over AoA and AoD as shown in (4), and $\rho_{lp,mq}$ is given by (9). Furthermore, $\mathbf{R}(\mathbf{\Lambda})$ is a $N_T N_R \times N_T N_R$ Hermitian block Toeplitz with Toeplitz blocks (H-BTTB) matrix. It has $N_T \times N_T$ blocks and each block is an $N_R \times N_R$ square matrix. A matrix is BTTB if its $(i,j)^{\text{th}}$ block is a function of $(i-j)$ and the $(i,j)^{\text{th}}$ block itself is a Toeplitz matrix. More discussion on BTTB matrices can be found in [29]. The Hermitian property is due to the Hermitian symmetry of the spatio-temporal cross correlation $\rho_{lp,mq}(\tau)$ around $\tau = 0$. The BTTB structure comes from the fact that $\rho_{lp,mq}(\tau) = \rho_{(l+i)(p+j),(m+i)(q+j)}(\tau), \forall i, j$. By taking advantage of the H-BTTB structure of $\mathbf{R}(\mathbf{\Lambda})$, the numerical search in (13) can be performed much faster, especially for large N_R and N_T.

Similarly, for the HUT data, $\mathbf{\Lambda}$ is estimated by fitting the spatio-temporal MIMO correlation matrix $\mathbf{R}(\mathbf{\Lambda}, k)$, whose elements are determined by (7), to the estimated spatio-temporal correlation matrix $\widehat{\mathbf{R}}(k)$

$$\widehat{\mathbf{\Lambda}} = \arg\min_{\mathbf{\Lambda}} \sum_{k=0}^{\tau_{\max}} \left\| \widehat{\mathbf{R}}(k) - \mathbf{R}(\mathbf{\Lambda}, k) \right\|_F^2 , \tag{14}$$

where $\tau_{\max}$ is set to 4 in the numerical search[11]. $\widehat{\mathbf{R}}(k) = T^{-1} \sum_{t=1}^{T} \mathbf{h}(t+k)\mathbf{h}^{\dagger}(t)$, $k \in [0, \tau_{\max}]$. $\mathbf{R}(\mathbf{\Lambda}, k) = \mathbb{E}[\mathbf{h}(t+k)\mathbf{h}^{\dagger}(t)]$ such that $[\mathbf{R}(\mathbf{\Lambda}, k)]_{l+N_R(p-1),m+N_R(q-1)} = \rho_{lp,mq}(k)$, $l, m \in [1, N_R]$ and $p, q \in [1, N_T]$. Note that $\rho_{lp,mq}(k)$ denotes $\rho_{lp,mq}(kT_s)$ given by (7). In addition, it is clearly seen that $\mathbf{R}(\mathbf{\Lambda}, 0)$ is an H-BTTB matrix, whereas for $k \neq 0$, $\mathbf{R}(\mathbf{\Lambda}, k)$ is a BTTB matrix. In a similar manner to (13), the parameter search in (14) can be sped up using the BTTB structure of $\mathbf{R}(\mathbf{\Lambda}, k)$.

It is clear from (9) that if μ and μ' are the outcomes of the search in (13), $2\beta_{lm} - \widehat{\mu}$ and $2\alpha_{pq} - \widehat{\mu}'$ are valid parameters as well and result in the same numerical values for (9). On the other hand, if μ' is the search result of (14), $2\alpha_{pq} - \widehat{\mu}'$ gives the same numerical value for (7) as well. All these angular ambiguities should be considered with the real propagation environments when looking at the search results of (13) and (14). Moreover, for the HUT

[10]The function in (13) is very complex since it depends on 7 free variables. The same observation applies to (14). Finding the optimal estimates is not the focus of this paper. This is a separate issue which is recently studied in [28].

[11]According to Appendix II, $\tau_{\max} = 4$ corresponds to $\frac{1}{f_D}$s.

TABLE I

ESTIMATED PARAMETER SETS FOR THE HUT AND BYU DATA

	$\widehat{\Delta}$	$\widehat{\Delta}'$	$\widehat{\kappa}$	$\widehat{\kappa}'$	$\widehat{\mu}$	$\widehat{\mu}'$	$\widehat{\eta}$
$\widehat{\mathbf{\Lambda}}_{\text{HUT}}$	$\frac{\pi}{6}$	$\frac{\pi}{4}$	17	2	$\frac{9\pi}{8}$	$\frac{15\pi}{8}$	0.7
$\widehat{\mathbf{\Lambda}}_{\text{BYU}}$	$\frac{\pi}{3}$	$\frac{\pi}{6}$	0	0.5	0	$\frac{5\pi}{8}$	0.2

data, the non-uniform antenna patterns [20, Fig. 2] were also considered when searching for parameters[7]. Finally, the estimated parameter sets for the HUT and BYU data are presented in Table I.

V. COMPARISON OF THE PROPOSED MODEL WITH COLLECTED DATA

This section presents the comparison of the proposed model with collected data in terms of various aspects of fading channels such as the statistical distribution of amplitude, phase, in-phase/quadrature components, spatial, temporal, and spatio-temporal correlations, level crossing rate, average fade duration, and MIMO mutual information.

A. Statistical Distribution of the Data

When deriving the compact spatio-temporal cross-correlation expression in (7), it has been assumed that the numbers of local scatterers around both the BS and MS are large enough. This translates into complex Gaussian distribution for each subchannel $h_{lp}(t)$ according to the central limit theorem [30]. To verify this, the data is normalized according to (12) such that each subchannel has zero mean with unit variance. As shown in Fig. 4, the real and imaginary parts of $h_{11}(t)$ of the HUT data are Gaussian. Furthermore, the empirical cumulative distribution functions (CDF) of the amplitude and phase are Rayleigh and uniform, respectively. The same types of plots are observed for other HUT subchannels, as well as the BYU data sets, as reported in [31, p. 162] and [32, Fig. 5].

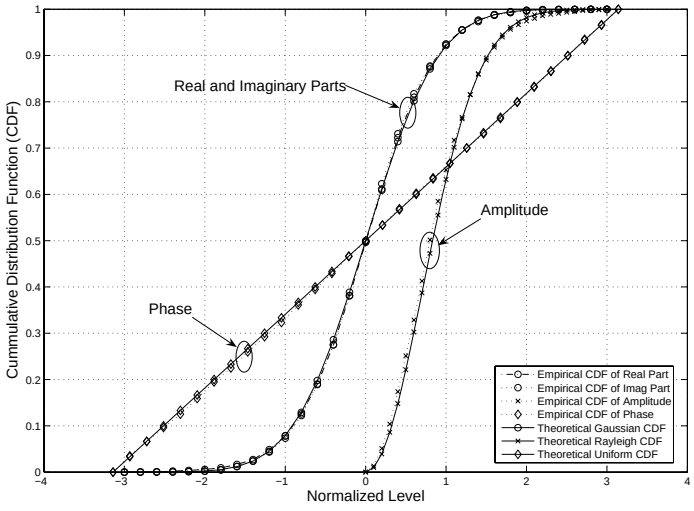

Fig. 4. Empirical and theoretical distributions of $h_{11}(t)$ in the HUT data.

B. Spatial Correlations

Here we consider four different types of spatial correlation, i.e., parallel, crossing, transmit, and receive correlations, defined by

$$\rho_{\text{parallel}} \triangleq \mathbb{E}[h_{lp}(t)h^{\star}_{(l+u)(p+u)}(t)], \tag{15a}$$

$$\rho_{\text{crossing}} \triangleq \mathbb{E}[h_{lp}(t)h^{\star}_{pl}(t)], \tag{15b}$$

$$\rho_{\text{Tx}} \triangleq \mathbb{E}[h_{lp}(t)h^{\star}_{lq}(t)], \tag{15c}$$

$$\rho_{\text{Rx}} \triangleq \mathbb{E}[h_{lp}(t)h^{\star}_{mp}(t)]. \tag{15d}$$

In a 2×2 channel, it can be shown that

$$\rho_{\text{parallel}} \triangleq \mathbb{E}[h_{11}(t)h^{*}_{22}(t)] = \rho_{11,22}, \tag{16}$$

$$\rho_{\text{crossing}} \triangleq \mathbb{E}[h_{12}(t)h^{*}_{2l}(t)] = \rho_{12,21}, \tag{17}$$

$$\rho_{\text{Tx}} \triangleq \mathbb{E}[h_{11}(t)h^{*}_{12}(t)] = \mathbb{E}[h_{21}(t)h^{*}_{22}(t)] = \rho_{11,12} = \rho_{21,22}, \tag{18}$$

$$\rho_{\text{Rx}} \triangleq \mathbb{E}[h_{11}(t)h^{*}_{21}(t)] = \mathbb{E}[h_{12}(t)h^{*}_{22}(t)] = \rho_{11,21} = \rho_{12,22}. \tag{19}$$

For the HUT data, the model correlations are obtained as (ρ_{parallel}, ρ_{crossing}, ρ_{Tx}, ρ_{Rx})=(0.01, 0.2, 0.5, 0.02) by plugging $\widehat{\mathbf{\Lambda}}_{\text{HUT}}$ from Table I into (9), whereas the empirical correlations are (0.04, 0.1, 0.6, 0.08) by processing the normalized data. For the BYU data, the same type of comparison for the above four correlations in terms of element spacing is shown in Fig. 5. The utility of the model is revealed by the close agreement between the model and empirical spatial correlations.

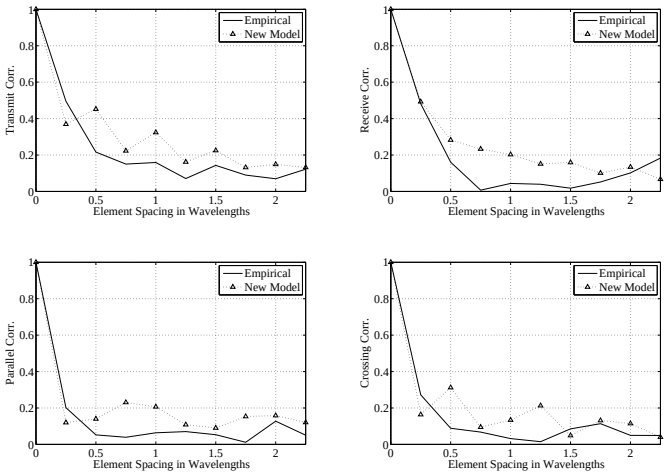

Fig. 5. Comparison of four different types of spatial correlations of the new MIMO model with the corresponding empirical correlations of the BYU data collected on 11/07/00.

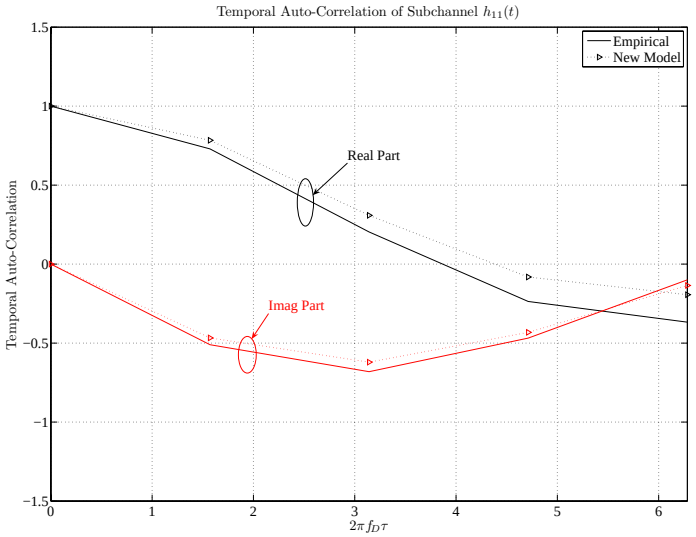

Fig. 6. The autocorrelation of $h_{11}(t)$, defined by $\mathbb{E}[h_{11}(t+\tau)h_{11}^{\star}(t)]$. New model and HUT data.

C. Spatio-Temporal Cross-Correlations

Fig. 6 shows the empirical autocorrelation of the subchannel $h_{11}(t)$ for the HUT data, together with the autocorrelation of the model obtained by plugging $\widehat{\mathbf{\Lambda}}_{\text{HUT}}$ of Table I into (8). The spatio-temporal cross-correlations of the HUT data between $h_{11}(t)$ & $h_{12}(t)$, and between $h_{12}(t)$ & $h_{11}(t)$, respectively, are shown in Figs. 7 and 8, where the cross-correlation of the model is plotted by substituting $\widehat{\mathbf{\Lambda}}_{\text{HUT}}$ of Table I into (7). The difference between the model cross-correlations in Figs. 7 and 8 is due to $\alpha_{21} = \alpha_{12} + \pi$, as explained in footnote 3. Clearly, the model provides a close fit to the empirical spatio-temporal correlations.

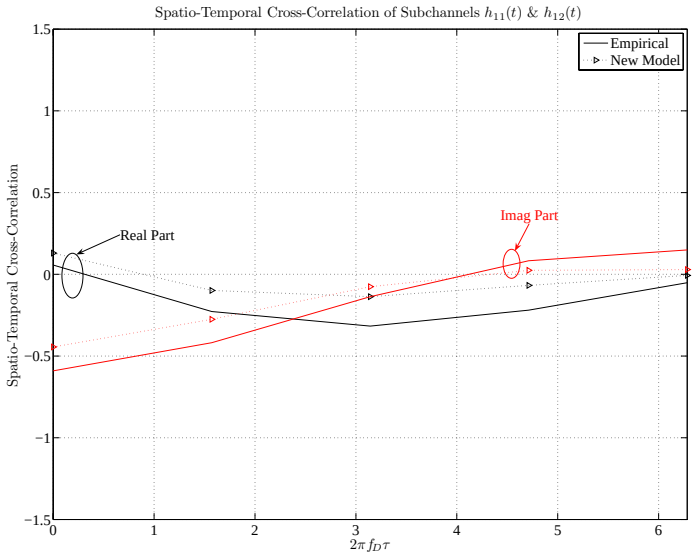

Fig. 7. The spatio-temporal cross-correlation between $h_{11}(t)$ and $h_{12}(t)$, defined by $\mathbb{E}[h_{11}(t+\tau)h_{12}^{\star}(t)]$. New model and HUT data.

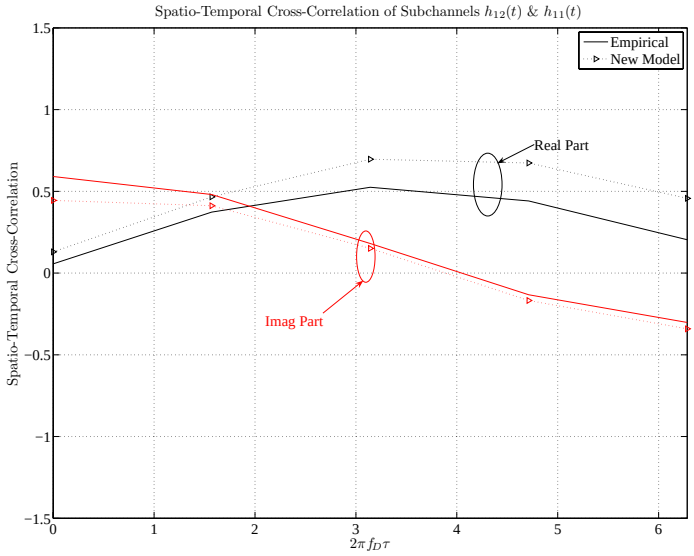

Fig. 8. The spatio-temporal cross-correlation between $h_{12}(t)$ and $h_{11}(t)$, defined by $\mathbb{E}[h_{12}(t+\tau)h_{11}^{\star}(t)]$. New model and HUT data.

D. Level Crossing Rate and Average Fade Duration

LCR and AFD of the signal envelope are two important temporal statistical features which provide useful information on the dynamic behavior of time-varying fading channels. To calculate the LCR and AFD of a subchannel, one needs its temporal autocorrelation. This is given in (8). With $\gamma = \frac{\pi}{2}$ in the HUT measurement campaign, (8) reduces to

$$\rho(\tau) = \frac{(1-\eta) I_0\left(\sqrt{\kappa'^2 - a^2\Delta'^2 - \jmath 2\kappa' a \Delta' \sin\mu'}\right)}{I_0(\kappa')} + \frac{\eta I_0\left(\sqrt{\kappa^2 - a^2 - \jmath 2\kappa a \sin\mu}\right)}{I_0(\kappa)}. \tag{20}$$

The k^{th} spectral moment $\mathcal{B}_k$ is defined by [33]

$$\mathcal{B}_k = \frac{d^k \rho(\tau)}{\jmath^k d\tau^k}\Big|_{\tau=0}, \tag{21}$$

which is also required for calculating LCR and AFD. From (20) and (21) we obtain

$$\mathcal{B}_0 = 1, \tag{22a}$$

$$\mathcal{B}_1 = 2\pi f_D \left[\frac{(1-\eta) I_1(\kappa')\Delta' \sin\mu'}{I_0(\kappa')} + \frac{\eta I_1(\kappa)\sin\mu}{I_0(\kappa)}\right], \tag{22b}$$

$$\mathcal{B}_2 = 4\pi^2 f_D^2 \left\{\eta\left[\sin^2\mu + \frac{I_1(\kappa)\cos(2\mu)}{\kappa I_0(\kappa)}\right] + (1-\eta)\Delta'^2\left[\sin^2\mu' + \frac{I_1(\kappa')\cos(2\mu')}{\kappa' I_0(\kappa')}\right]\right\}. \tag{22c}$$

The theoretical LCR and AFD at the given threshold r for Rayleigh fading are respectively given by [33]

$$N_{|h|}(r) = \sqrt{\frac{\mathcal{B}_2 - \mathcal{B}_1^2}{\pi}} r e^{-r^2}, \tag{23}$$

and

$$\bar{t}_{|h|}(r) = \frac{\sqrt{\pi}\left(e^{r^2} - 1\right)}{r\sqrt{\mathcal{B}_2 - \mathcal{B}_1^2}}, \tag{24}$$

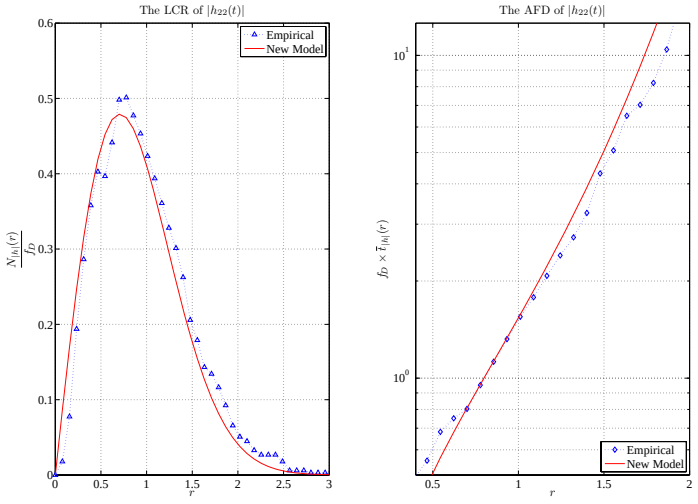

Fig. 9. LCR and AFD of $h_{22}(t)$. New model and HUT data.

where $|h|$ denotes the amplitude of any subchannel.

By plugging the estimated parameter set $\widehat{\mathbf{\Lambda}}_{\text{HUT}}$ of Table I into (23) and (24), the LCR and AFD of the model are compared in Fig. 9 with the empirical LCR and AFD of $|h_{22}(t)|$, versus r. The close match for this and three other subchannels, not shown due to space limitation, verifies the ability of the model in capturing the dynamics of the channel.

E. CDF of Instantaneous Mutual Information

In this subsection, we focus on the instantaneous mutual information (IMI) under equal-power transmission to verify our proposed model. Assuming that the channel matrix $\mathbf{H}(t)$ is known at the receiver but not at the transmitter, with the MIMO channel characterized in (1), the IMI under equal-power transmission, in bits/s/Hz, is given by [2]

$$\mathcal{I}(t) = \log_2 \det\left(\mathbf{I}_{N_R} + \frac{P_{\text{Tx}}}{N_T P_{\text{Noise}}}\mathbf{H}(t)\mathbf{H}^{\dagger}(t)\right), \tag{25}$$

where $\det(\cdot)$ is the matrix determinant. Note that at any time instant t, $\mathcal{I}(t)$ is a random variable, and its distribution depends on the distribution of the random matrix $\mathbf{H}(t)\mathbf{H}^{\dagger}(t)$. In this paper, we compare the empirical distribution of the MIMO IMI of the data, with the distribution predicted by our proposed model, where the SNR $= P_{\text{Tx}}/P_{\text{Noise}}$ is set to 20dB in (25). In Figs. 10 and 11, three different CDFs of IMI are plotted for the HUT and BYU data, respectively. The "Empirical" IMI is calculated using (25) directly from the collected snapshots $\{\mathbf{H}(t)\}_{t=1}^{T}$. However, for each of the other IMIs, first a zero-mean $N_R \times N_T$ Gaussian matrix $\mathbf{H}_{\text{IID}}$ with i.i.d elements is generated for each t such that $\mathbf{h}_{\text{IID}} = \text{vec}(\mathbf{H}_{\text{IID}})$ and $\mathbb{E}[\mathbf{h}_{\text{IID}}\mathbf{h}_{\text{IID}}^{\dagger}] = \mathbf{I}_{N_R N_T}$. The "IID" IMI CDF is obtained by inserting $\mathbf{H}_{\text{IID}}$ into (25). To obtain the "New Model" IMI CDF, the following necessary steps are done.

- For the HUT data, the correlated matrix-valued random process $\mathbf{H}(t)$ is generated using the spectral method [34], based on (7) and $\widehat{\mathbf{\Lambda}}_{\text{HUT}}$ of Table I, and then plugged into (25).

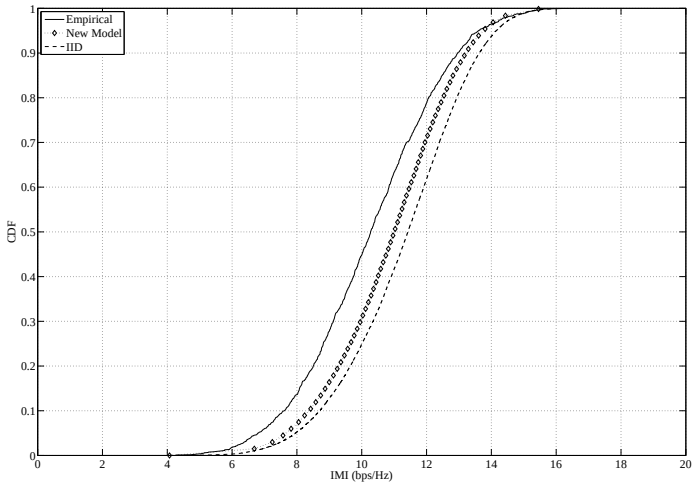

Fig. 10. Distributions of the IMI: HUT data.

- For the BYU data, the colored Gaussian vector $\mathbf{h}\left(\widehat{\mathbf{\Lambda}}_{\text{BYU}}\right)$ is built according to $\mathbf{h}\left(\widehat{\mathbf{\Lambda}}_{\text{BYU}}\right) = \sqrt{\mathbf{R}\left(\widehat{\mathbf{\Lambda}}_{\text{BYU}}\right)}\mathbf{h}_{\text{IID}}$, where $\sqrt{\mathbf{R}\left(\widehat{\mathbf{\Lambda}}_{\text{BYU}}\right)}$ is the Cholesky matrix of $\mathbf{R}\left(\widehat{\mathbf{\Lambda}}_{\text{BYU}}\right)$, $\mathbf{R}(\mathbf{\Lambda})$ is defined in Subsection IV-B, and $\widehat{\mathbf{\Lambda}}_{\text{BYU}}$ is given in Table I. Then the channel matrix $\mathbf{H}\left(\widehat{\mathbf{\Lambda}}_{\text{BYU}}\right)$ is generated from $\mathbf{h}\left(\widehat{\mathbf{\Lambda}}_{\text{BYU}}\right) = \text{vec}\left(\mathbf{H}\left(\widehat{\mathbf{\Lambda}}_{\text{BYU}}\right)\right)$ and substituted in (25).

According to Figs. 10 and 11, the model fits the HUT data well. However, the match to the BYU data is not as good as the HUT data. This may be partly because the assumption $D \gg \max(R', R)$ does not strictly hold for the scenarios where the BYU data was collected.

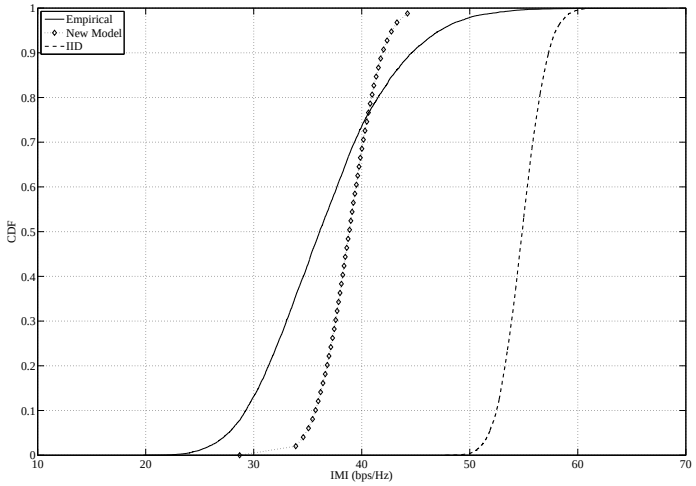

Fig. 11. Distributions of the IMI: BYU data.

VI. Conclusion

In this paper, a parametric statistical MIMO model is proposed where both the base and mobile stations experience local scattering. The model yields a closed-form and mathematically-tractable expression for the spatio-temporal cross-correlation between any two subchannels of a MIMO system with arbitrary transmit and receive array configurations. The model includes some key physical channel parameters such as the mean angle-of-departure and angle-of-arrival, angle spreads, maximum Doppler frequency, sizes of the local scattering rings, and the relative contribution of BS and MS local scatterers.

The proposed model is general enough to include, as special cases, most existing correlation models such as the MIMO model of [3], Lee's spatio-temporal correlation model and Clarke's classical spatial/temporal correlation model with isotropic scattering. Comparison of the model with outdoor and indoor collected data, in terms of spatial correlations, temporal autocorrelations, spatio-temporal cross-correlations, level crossing rates, average fade duration, and the distribution of mutual information has demonstrated the flexibility of the model in describing real-world propagation environments. The proposed model, supported by empirical observation, provides a useful channel characterization required for efficient design and performance prediction of multi-antenna transceivers.

Acknowledgement

The authors thank anonymous reviewers for their careful reviews of the paper. Their comments have certainly improved the quality of the paper.

Appendix I
Derivation of (5) and (7)

Based on the application of the law of cosines in appropriate triangles in Fig. 2 we obtain

$$\xi_{px}'^2 = \delta_{pq}^2/4 + R'^2 - \delta_{pq} R' \cos(\alpha_{pq} - x), \tag{26a}$$

$$\xi_{qx}'^2 = \delta_{pq}^2/4 + R'^2 + \delta_{pq} R' \cos(\alpha_{pq} - x), \tag{26b}$$

$$\xi_{xl}'^2 = d_{lm}^2/4 + \xi_x'^2 - \xi_x' d_{lm} \cos(v - \beta_{lm}), \tag{26c}$$

$$\xi_{xm}'^2 = d_{lm}^2/4 + \xi_x'^2 + \xi_x' d_{lm} \cos(v - \beta_{lm}), \tag{26d}$$

$$\xi_{py}^2 = \delta_{pq}^2/4 + \xi_y^2 - \xi_y \delta_{pq} \cos(\alpha_{pq} - w), \tag{26e}$$

$$\xi_{qy}^2 = \delta_{pq}^2/4 + \xi_y^2 + \xi_y \delta_{pq} \cos(\alpha_{pq} - w), \tag{26f}$$

$$\xi_{yl}^2 = d_{lm}^2/4 + R^2 - d_{lm} R \cos(y - \beta_{lm}), \tag{26g}$$

$$\xi_{ym}^2 = d_{lm}^2/4 + R^2 + d_{lm} R \cos(y - \beta_{lm}), \tag{26h}$$

where to simplify the notation, we use x for ϕ_k', y for ϕ_i, v for φ_k', w for φ_i, ξ_x' for ξ_k', and ξ_y for ξ_i.

The following identity can be obtained by subtracting (26b) from (26a)

$$\xi_{px}' - \xi_{qx}' = \frac{-2\delta_{pq} R' \cos(\alpha_{pq} - x)}{\xi_{px}' + \xi_{qx}'}. \tag{27}$$

With the assumption of $R' \gg \delta_{pq}$, we have $\xi'_{px} + \xi'_{qx} \approx 2R'$, therefore, (27) reduces to

$$\xi'_{px} - \xi'_{qx} \approx -\delta_{pq} \cos(\alpha_{pq} - x). \tag{28}$$

By applying the same reasoning to (26c)-(26h) and using the assumptions $D \gg \max(R', R)$ and $R \gg d_{lm}$, which imply $\xi'_{xl} + \xi'_{xm} \approx 2\xi'_x$, $\xi_{py} + \xi_{qy} \approx 2\xi_y$, and $\xi_{yl} + \xi_{ym} \approx 2R$, we obtain the following approximations

$$\xi'_{xl} - \xi'_{xm} \approx -d_{lm} \cos(v - \beta_{lm}), \tag{29a}$$

$$\xi_{py} - \xi_{qy} \approx -\delta_{pq} \cos(\alpha_{pq} - w), \tag{29b}$$

$$\xi_{yl} - \xi_{ym} \approx -d_{lm} \cos(y - \beta_{lm}). \tag{29c}$$

Substitution of (28) and (29) into (4) results in the integral representation (5).

Now we apply the law of sines to the triangles $O'S'_kO$ and $O'S_iO$, respectively, to obtain the following identities

$$\frac{D}{\sin(v - x)} = \frac{R'}{\sin(\pi - v)}, \tag{30a}$$

$$\frac{D}{\sin(y - w)} = \frac{R}{\sin w}. \tag{30b}$$

From Fig. 2, it is clear that $\pi - v \leqslant \Delta'$, $w \leqslant \Delta$, $\Delta' = \arcsin \frac{R'}{D}$, and $\Delta = \arcsin \frac{R}{D}$. Based on the assumption $D \gg \max(R', R)$, we conclude that Δ' and Δ, and consequently $\pi - v$ and w are small quantities. This observation, together with $\sin \epsilon \approx \epsilon$ when ϵ is small, allow us to derive the following approximations from (30a) and (30b)

$$v \approx \pi - \Delta' \sin x, \tag{31a}$$

$$w \approx \Delta \sin y. \tag{31b}$$

Furthermore, using $\sin \epsilon \approx \epsilon$ and $\cos \epsilon \approx 1$ when ϵ is small, together with (31a) and (31b), $\cos(v - \beta_{lm})$ and $\cos(\alpha_{pq} - w)$ can be approximated as

$$\cos(v - \beta_{lm}) \approx -\cos \beta_{lm} + \Delta' \sin \beta_{lm} \sin x, \tag{32a}$$

$$\cos(\alpha_{pq} - w) \approx \cos \alpha_{pq} + \Delta \sin \alpha_{pq} \sin y. \tag{32b}$$

By plugging (6b), (6a), (32a) and (32b) into (5), and calculating the two integrals according to [35, 3.338-4]

$$\int_{-\pi}^{\pi} \exp(x \sin\theta + y \cos\theta) d\theta = 2\pi I_0\left(\sqrt{x^2 + y^2}\right), \tag{33}$$

the general spatio-temporal cross-correlation in (7) can be obtained, after some algebraic manipulations.

APPENDIX II
HUT DATA

Fig. 12 shows the layout of the location where the HUT data is collected. The 2×2 measurement setup and four subchannels are shown in Fig. 13(a), whereas the configuration of the Rx array is presented in Fig. 13(b). The Tx and Rx element spacings are given by $\delta_{12} = \lambda$ and $d_{12} = 2.785\lambda$, respectively. The mobile speed is 0.4 m/s, which with the $2.154\,$GHz carrier frequency result in $f_D = \nu/\lambda = 2.872\,$Hz. There are $T = 1342$ snapshots of

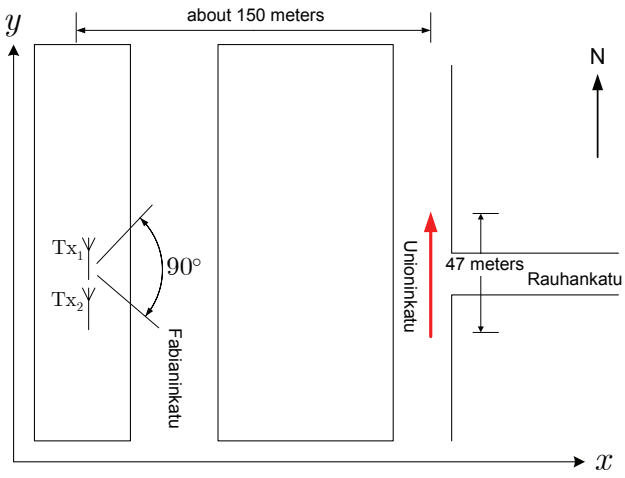

Fig. 12. The layout of the environment campaign of the HUT data.

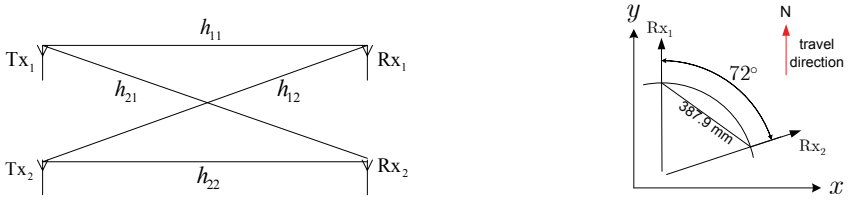

(a) The 2×2 system (b) Receiver array

Fig. 13. The measurement setup for the HUT data.

the channel matrix $\mathbf{H}(t)$, and any two adjacent snapshots are separated by $\frac{\lambda}{4}$ in space, equivalent to 87.05 ms in time. Further details of the data and measurement setup can be found in [19] and [20]. The pathloss is removed from the data by least-squares fitting of a 10^{th} order polynomial in the dB domain, and the power normalization is performed according to (12).

APPENDIX III
BYU DATA

For the data collected on $11/07/00$ at BYU, the room layout is shown in Fig. 14. Both the Tx and Rx arrays are linear, each with 10 monopole elements and $\lambda/4$ spacing, at the carrier frequency of $2.42\,\text{GHz}$. The Tx array was placed at 4 different locations in room 484, whereas the Rx array was placed at 6 different locations in room 400. There are 24 Tx-Rx location configurations, 20 data sets per location, and 124 snapshots of the 10×10 channel matrix per data set. Power normalization of each data set was done according to

$$\tilde{h}_{loc,set,lp}(t) = \frac{h_{loc,set,lp}(t) - \widehat{m}_{loc,set,lp}}{\widehat{\sigma}_{loc,set,lp}}, set \in [1,20], l,p \in [1,10], t \in [1,124], \tag{34}$$

where loc is the location index $\{1\_1, \cdots, 1\_6, 2\_1, \cdots, 2\_6, 3\_1, \cdots, 3\_6, 4\_1, \cdots, 4\_6\}$, set is the data set index at each location, and $\widehat{m}_{loc,set,lp}$ and $\widehat{\sigma}^2_{loc,set,lp}$ are the estimated mean and variance of the subchannel $h_{lp}(t)$ in the set^{th}

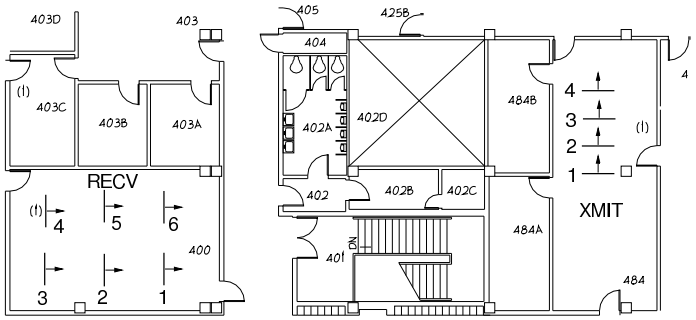

Fig. 14. The room layout where the BYU data is collected. In the figure, "$\overset{\uparrow}{\text{—}}$" denotes 10 antenna elements are numbered as $\overset{\uparrow}{1,\cdots,10}$.

data set at the loc^{th} location. Because of the fixed Tx and Rx and stationary environment we have $f_D = 0\,\text{Hz}$. More measurement information can be found in [31, Chap. 6-7] and [32], where this data set is labeled as "$10\times10(a)$".

REFERENCES

[1] G. J. Foschini and M. J. Gans, "On limits of wireless communications in a fading environment when using multiple antennas," *Wireless Personal Commun.*, vol. 6, pp. 311–335, 1998.

[2] İ. E. Telatar, "Capacity of multi-antenna Gaussian channels," *European Trans. Telecommun.*, vol. 10, pp. 585–595, 1999.

[3] A. Abdi and M. Kaveh, "A space-time correlation model for multielement antenna systems in mobile fading channels," *IEEE J. Select. Areas Commun.*, vol. 20, pp. 550–560, Apr. 2002.

[4] P. J. Smith, S. Roy, and M. Shafi, "Capacity of MIMO systems with semicorrelated flat fading," *IEEE Trans. Inform. Theory*, vol. 49, pp. 2781–2788, Oct. 2003.

[5] M. Chiani, M. Z. Win, and A. Zanella, "On the capacity of spatially correlated MIMO Rayleigh-fading channels," *IEEE Trans. Inform. Theory*, vol. 49, pp. 2363–2371, Oct. 2003.

[6] A. Goldsmith, S. A. Jafar, N. Jindal, and S. Vishwanath, "Capacity limits of MIMO channels," *IEEE J. Select. Areas Commun.*, vol. 21, pp. 684–702, June 2003.

[7] D. P. Liu, Q. T. Zhang, and Q. Chen, "Structures and performance of noncoherent receivers for unitary space-time modulation on correlated fast-fading channels," *IEEE Trans. Veh. Technol.*, vol. 53, pp. 1116–1125, July 2004.

[8] G. Femenias, "BER performance of linear STBC from orthogonal designs over MIMO correlated Nakagami-m fading channels," *IEEE Trans. Veh. Technol.*, vol. 53, pp. 307–317, Mar. 2004.

[9] V. K. Nguyen and L. B. White, "Joint space-time trellis decoding and channel estimation in correlated fading channels," *IEEE Signal Processing Lett.*, vol. 11, pp. 633–636, July 2004.

[10] M. Jankiraman, *Space-Time Codes and MIMO Systems*. Boston, MA: Artech House, 2004.

[11] K. Yu and B. Ottersten, "Models for MIMO propagation channels: A review," *Wirel. Commun. Mob. Comput.*, vol. 2, pp. 653–666, 2002.

[12] A. Abdi, "Stochastic modeling and simulation of multiple-input multiple-output channels: A unified approach," in *Proc. IEEE Int. Symp. Antennas Propagat.*, Monterey, CA, 2004, pp. 3673–3676.

[13] A. F. Molisch, "A generic model for MIMO wireless propagation channels in macro- and microcells," *IEEE Trans. Signal Processing*, vol. 52, pp. 61–71, Jan. 2004.

[14] M. A. Jensen and J. W. Wallace, "A review of antennas and propagation for MIMO wireless communications," *IEEE Trans. Antennas Propagat.*, vol. 52, pp. 2810–2824, Nov. 2004.

[15] M. Steinbauer, D. Hampicke, G. Sommerkorn, A. Schneider, A. F. Molisch, R. Thoma, and E. Bonek, "Array measurement of the double-directional mobile radio channel," in *Proc. IEEE Veh. Technol. Conf.*, Tokyo, Japan, 2000, pp. 1656–1662.

[16] M. Steinbauer, A. F. Molisch, and E. Bonek, "The double-directional radio channel," *IEEE Antennas Propagat. Mag.*, vol. 43, pp. 51–63, Aug. 2001.

[17] S. Savazzi, O. Simeone, and U. Spagnolini, “Optimal design of linear arrays in a TDMA cellular system with Gaussian interference,” in *Proc. IEEE Int. Workshop Signal Processing Advances in Wireless Communications*, New York, 2005, pp. 485–489.

[18] D. Gesbert, H. Bolcskei, D. A. Gore, and A. J. Paulraj, “Outdoor MIMO wireless channels: models and performance prediction,” *IEEE Trans. Commun.*, vol. 50, pp. 1926–1934, Dec. 2002.

[19] K. Sulonen, P. Suvikunnas, J. Kivinen, L. Vuokko, and P. Vainikainen, “Study of different mechanisms providing gain in MIMO systems,” in *Proc. IEEE Veh. Technol. Conf.*, Orlando, FL, 2003, pp. 352–356.

[20] K. Kalliola, H. Laitinen, L. I. Vaskelainen, and P. Vainikainen, “Real-time 3-D spatial-temporal dual-polarized measurement of wideband radio channel at mobile station,” *IEEE Trans. Instrum. Meas.*, vol. 49, pp. 439–448, Apr. 2000.

[21] J. W. Wallace and M. A. Jensen, “Measured characteristics of the MIMO wireless channel,” in *Proc. IEEE Veh. Technol. Conf.*, Atlantic City, NJ, 2001, pp. 2038–2042.

[22] The MIMO data@BYU. [Online]. Available: http://ee.byu.edu/wireless/

[23] A. Abdi, J. A. Barger, and M. Kaveh, “A parametric model for the distribution of the angle of arrival and the associated correlation function and power spectrum at the mobile station,” *IEEE Trans. Veh. Technol.*, vol. 51, pp. 425–434, May 2002.

[24] G. L. Stüber, *Principles of Mobile Communications*, 2nd ed. Boston: Kluwer, 2000.

[25] T. L. Fulghum, K. J. Molnar, and A. Duel-Hallen, “The Jakes fading model for antenna arrays incorporating azimuth spread,” *IEEE Trans. Veh. Technol.*, vol. 51, pp. 968–977, Sept. 2002.

[26] J. W. Wallace and M. A. Jensen, “Modeling the indoor MIMO wireless channel,” *IEEE Trans. Antennas Propagat.*, vol. 50, pp. 591–599, May 2002.

[27] K. Yu, M. Bengtsson, B. Ottersten, D. McNamara, P. Karlsson, and M. Beach, “Second order statistics of NLOS indoor MIMO channels based on 5.2 GHz measurements,” in *Proc. IEEE Global Telecommun. Conf.*, San Antonio, TX, 2001, pp. 156–160.

[28] C. B. Ribeiro, E. Ollila, and V. Koivunen, “Propagation parameter estimation in MIMO systems using mixture of angular distributions model,” in *Proc. IEEE Int. Conf. Acoust., Speech, Signal Processing*, Philadelphia, PA, 2005, pp. 18–23.

[29] N. K. Bose and K. J. Boo, “Asymptotic eigenvalue distribution of block-toeplitz matrices,” *IEEE Trans. Inform. Theory*, vol. 44, pp. 858–861, Mar. 1998.

[30] A. Papoulis and S. U. Pillai, *Probability, Random Variables and Stochastic Processes*, 4th ed. New York: McGraw-Hill Higher Education, 2001.

[31] J. W. Wallace, “Modeling electromagnetic wave propagation in electrically large structures,” Ph.D. dissertation, Brigham Young Univ., Provo, UT, 2002.

[32] J. W. Wallace, M. A. Jensen, A. L. Swindlehurst, and B. D. Jeffs, “Experimental characterization of the MIMO wireless channel: data acquisition and analysis,” *IEEE Trans. Wireless Commun.*, vol. 2, pp. 335–343, Mar. 2003.

[33] A. Abdi, K. Wills, H. A. Barger, M. S. Alouini, and M. Kaveh, “Comparison of the level crossing rate and average fade duration of Rayleigh, Rice, and Nakagami fading models with mobile channel data,” in *Proc. IEEE Veh. Technol. Conf.*, Boston, MA, 2000, pp. 1850–1857.

[34] K. Acolatse and A. Abdi, “Efficient simulation of space-time correlated MIMO mobile fading channels,” in *Proc. IEEE Veh. Technol. Conf.*, Orlando, FL, 2003, pp. 652–656.

[35] I. S. Gradshteyn, I. M. Ryzhik, and A. Jeffrey, Eds., *Table of Integrals, Series, and Products*, 5th ed. San Diego, CA: Academic, 1994.